ACS OMEGA

http://pubs.acs.org/journal/acsodf

Article

Petrophysics of Kerogens Based on Realistic Structures

Saad Alafnan*

Cite This: *ACS Omega* 2021, 6, 9549−9558

Read Online

ACCESS | Metrics & More | Article Recommendations

ABSTRACT: Combining hydraulic fracturing with lateral drilling has allowed for economical hydrocarbon production from unconventional formations. Nevertheless, beyond hydraulic fracturing, our understanding of how hydrocarbons are stored and transported from the stimulated volume of a reservoir is still limited. Source rocks consist of organic materials finely dispersed within an inorganic matrix. Despite their small size, these organic pockets are capable of storing significant amounts of hydrocarbon due to their large surface area. The extent of the source rock's storage capacity is determined by several factors, including the natural fracture abundancy, organic material content, type, and level of maturity. The petrophysical properties of organic materials, also known as kerogens, are subject to a high degree of uncertainty. Kerogens are difficult to isolate experimentally, which hinders accurate petrophysical analysis. The objective of this research was to use a molecular modeling approach to explore the petrophysical characteristics of kerogen. Kerogen macromolecules of different types and maturity levels were recreated via a computational platform. Then nanoporous structures representing these kerogens were obtained and characterized. Several elemental parameters, including porosity, density, pore size distribution, and adsorption capacity were closely delineated. The kerogen properties were found to correlate with the kerogen type and thermal maturity level. Kerogen type III showed the highest storage capacity, followed by types II and I, in a descending order. Moreover, in the same type of kerogen, a general trend of increasing storage capacity was observed as the maturity level increased. Methane adsorption capacity was modeled as a function of kerogen porosity. A transition flow regime was found to be the predominant mechanism. Such observations have significant implications for reservoir-scale modeling of unconventional resources.

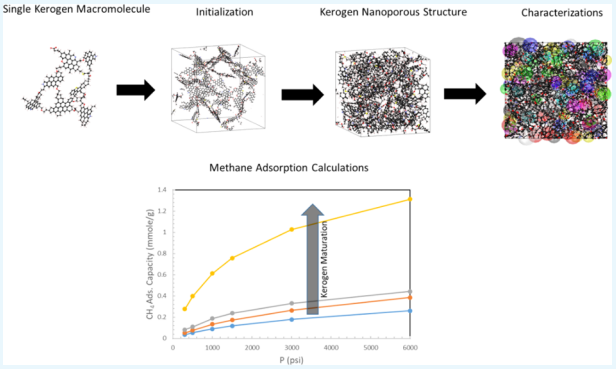

INTRODUCTION

Production stimulation techniques such as combining hydraulic fracturing and lateral drilling have made exploiting unconventional formations economically feasible. These advancements in production are not, however, necessarily accompanied by a clear understanding of the transport and storage mechanisms within a source rock matrix.

Source rocks, which are clastic sedimentary rocks composed of a complex mineralogy of clay, quartz, calcite, and fragments of organic materials, are tight formations. Their intrinsic permeability can primarily be attributed to natural fractures induced by tectonic movement.[1,2] Another constituent of source rock is the organic matter consisting of kerogen and bitumen. The latter is soluble in organic solvents, while the former represents a solid, best thought of as a nanoporous material.[3−6]

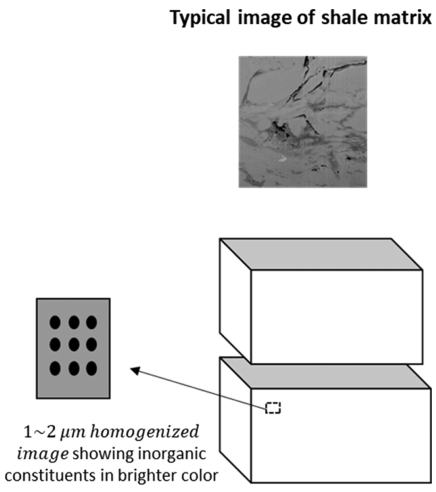

Figure 1. Schematic of shale samples showing organic materials finely dispersed within an inorganic matrix.

Received: January 3, 2021
Accepted: March 17, 2021
Published: March 30, 2021

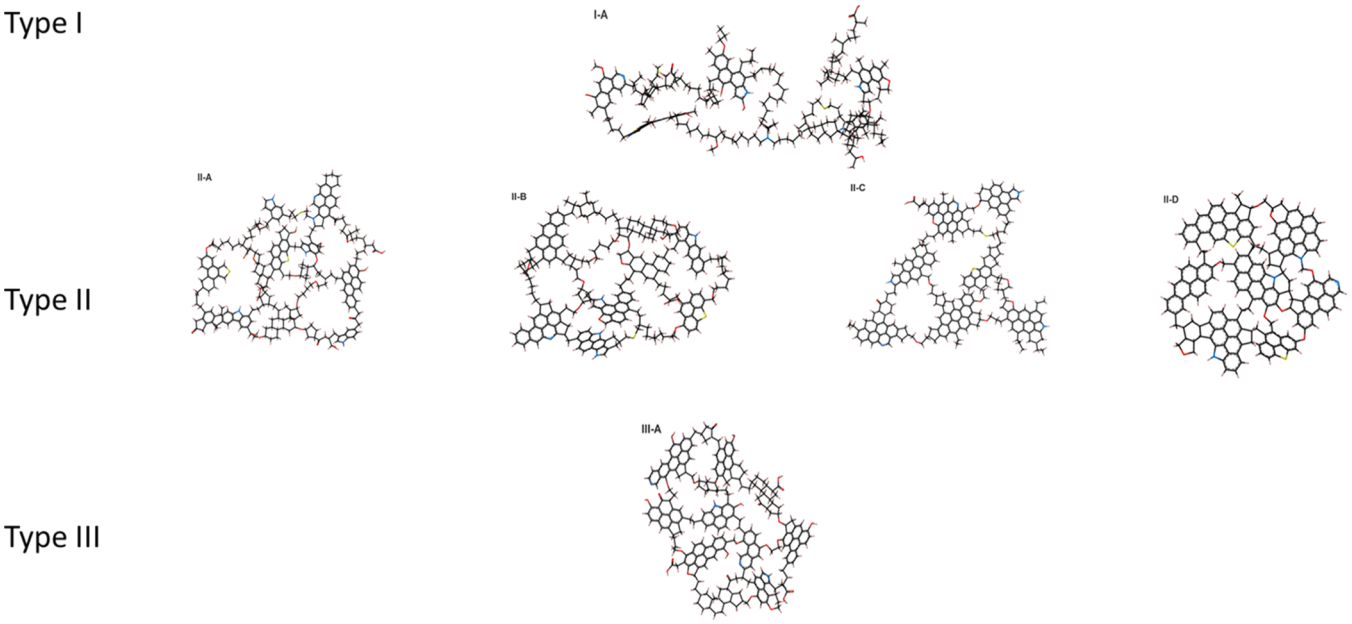

Figure 2. Six kerogen macromolecules recreated on a computational platform.[28]

Kerogens are capable of storing significant amounts of sorbed and free hydrocarbons due to their relatively large surface area.[7] The length scale of organic materials, usually a few nanometers, deviates from the continuum of fluid mechanics and thermodynamics. Scanning electron microscopy (SEM) images of source rocks reveal finely dispersed organic materials of a dark color within an inorganic matrix (see Figure 1). Chemical and physical properties change with the kerogen type and level of maturation. Origin and maturity levels can both play important roles in determining the storage capacity of shale formations. Experimental characterization of such organic pockets requires extraction, followed by typical petrophysical measurements; this is a challenging task accompanied by a high degree of uncertainty. Alternatively, molecular representation on a virtual platform can be used to simulate transport and storage capacity for assessment purposes.

The presence of micropores increases porosity and hence, the adsorption capacity of source rocks. The abundancy of such micropores has been experimentally investigated for different kerogen types across a range of thermal maturity levels. Zhang et al.[8] measured the porosity of shale, finding it to be higher in the presence of overmature kerogen. The increase in porosity was attributed to the high level of maturity.[9] Conversely, the presence of micropores was observed to be insignificant in low-maturity samples.[10] In sum, experimental investigations have showed that the presence of micropores can be linked to TOC, with their concentration being determined by the degree of organic materials and level of maturation. However, the degree of confinement and a complex mineralogy restrict direct assessment of kerogen's petrophysical characteristics. The goal of the present research is to overcome the limitations of current experimental approaches and place greater emphasis on the petrophysics of kerogens. In particular, properties such as porosity, pore size distribution (PSD), and methane adsorption capacity are delineated below for three major types of kerogen.

Efforts to classify kerogens began in the 1940s. It was observed that kerogens appearing in coal formations were almost indistinguishable from the matrix itself (due to the graphene-like structure), while those present in other sedimentary rocks were more aliphatic.[11,12] Modern classifications are based on elemental analysis. In particular, the ratios of hydrogen to carbon (H/C) and oxygen to carbon (O/C) can be linked to the degree of aromaticity and oxidation level. Hence, kerogens can be ordered by the level of maturity.[13,14] In general, kerogens are classified as types I, II, III, and IV. Within each type exists a range of maturity levels.[14,15] In some references, type IV is combined with type III to comprise a single class.[16] Type I is highly aliphatic, with a ratio greater than 1.5 and an O/C ratio below 0.1.[16] Type II contains a larger amount of cyclic aliphatic constituents and aromatics, which is reflected in the decreasing H/C ratio.[17] Type III, which is deposited in shallow marine environments, is vulnerable to further oxidation and thus increased oxygen content, either as functional groups or bonding cyclic chains of aromatics and cyclic aliphatic moieties.[17,18]

Forsman[19] was the first to model the kerogen structure through functional group characterization. He recognized two distinct groups. The first exhibited a condensed aromatic structure fused by functional groups such as ether or alkoxy. Hypothetical macromolecular models matching the elemental ratios were approximated based on arbitrary building blocks.[20−23] However, these models failed to match the measured density of kerogens, indicating a lack of representative 3D spatial configurations.[24] Some advancements in representing kerogen structures at different maturity levels have been achieved, beginning with the type I model.[25] This was followed by three type II structures: diagenesis, the beginning of catagenesis, and the end of catagenesis.[26] With advancements in computer-assisted modeling techniques, more representative porotypes of kerogen structures were generated, such as the six different models including types IA, IIA, IIB, IIC, IID, and IIIA.[27,28] In general, the aforementioned studies were conducted to generate synthetic models that could reproduce some of the macroscopic properties of kerogens but cannot be regarded as exact replications of those that are naturally occurring.

MOLECULAR APPROACH

Construction of Nanoporous Kerogen Structures. To investigate the petrophysical properties of kerogen, a repre-

https://doi.org/10.1021/acsomega.1c00018
ACS Omega 2021, 6, 9549−9558

Table 1. Elemental Kerogen Ratios by Ungerer[28]

kerogen type	maturity level	H/C	O/C	N/C	S/C	aromatic carbon (%)
KIA	immature	1.530	0.052	0.028	0.012	29
KIIA	immature	1.170	0.095	0.024	0.012	41
KIIB	top of oil window	1.120	0.060	0.022	0.009	45
KIIC	middle—end of oil window	0.905	0.054	0.021	0.008	59
KIID	overmature	0.580	0.051	0.023	0.011	79
KIIIA	immature	0.870	0.116	0.017	0.000	57

sentative structure exemplifying kerogen is required to serve as nanoporous media. In this research, we employed a novel molecular modeling technique to recreate the nanoporous structure of kerogen on a virtual platform. Extracting kerogen in amounts sufficient for petrophysical assessments is laborious and generally requires the application of strong acids and/or thermal treatments. Molecular simulation has become a viable alternative for studying kerogen under pressure and temperature conditions that might be impossible using lab-based approaches. Furthermore, a molecular modeling approach offers unprecedented flexibility in analysis of, for example, different functional groups, bonding strengths, and other chemical properties. The petrophysical analysis performed in this study relied on the novel work on six kerogen units configured by Ungerer et al.[28] These

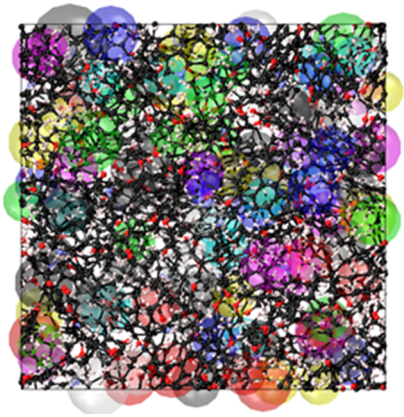

Figure 4. Sample visual illustration of the PSD algorithm performed for one of the kerogen structures. Changes in color reflect changes in pore size, where larger spheres were depicted in lighter colors.

macromolecules encompass the basic kerogen types (see Figure 2 and Table 1). To perform the petrophysical assessments, it was essential to maintain proper 3D spatial configurations, ensuring that physical properties such as density remained consistent with the experimental data.

Kerogen macromolecules IA, IIA, IIB, IIC, IID, and IIID were recreated at a molecular level, as shown in Figure 2. A polymer-consistent force field (PCFF+), which is known for its ability to model the atomic constituents of kerogen, was used to assign the

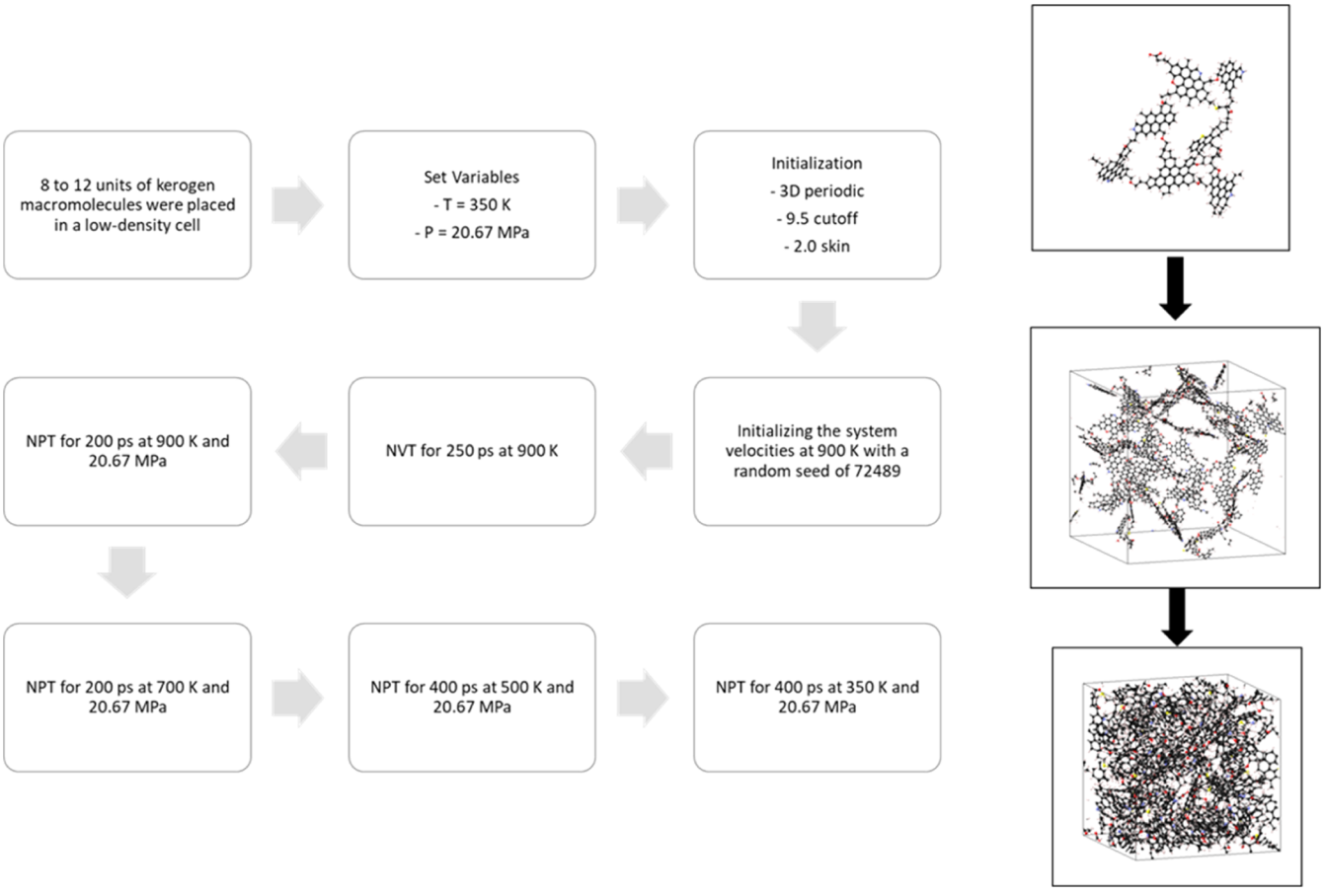

Figure 3. Left: LAMMPS protocol workflow for the creation of kerogen nanostructures. Right: Progression from a single kerogen unit to the final kerogen structure.

https://doi.org/10.1021/acsomega.1c00018
ACS Omega 2021, 6, 9549−9558

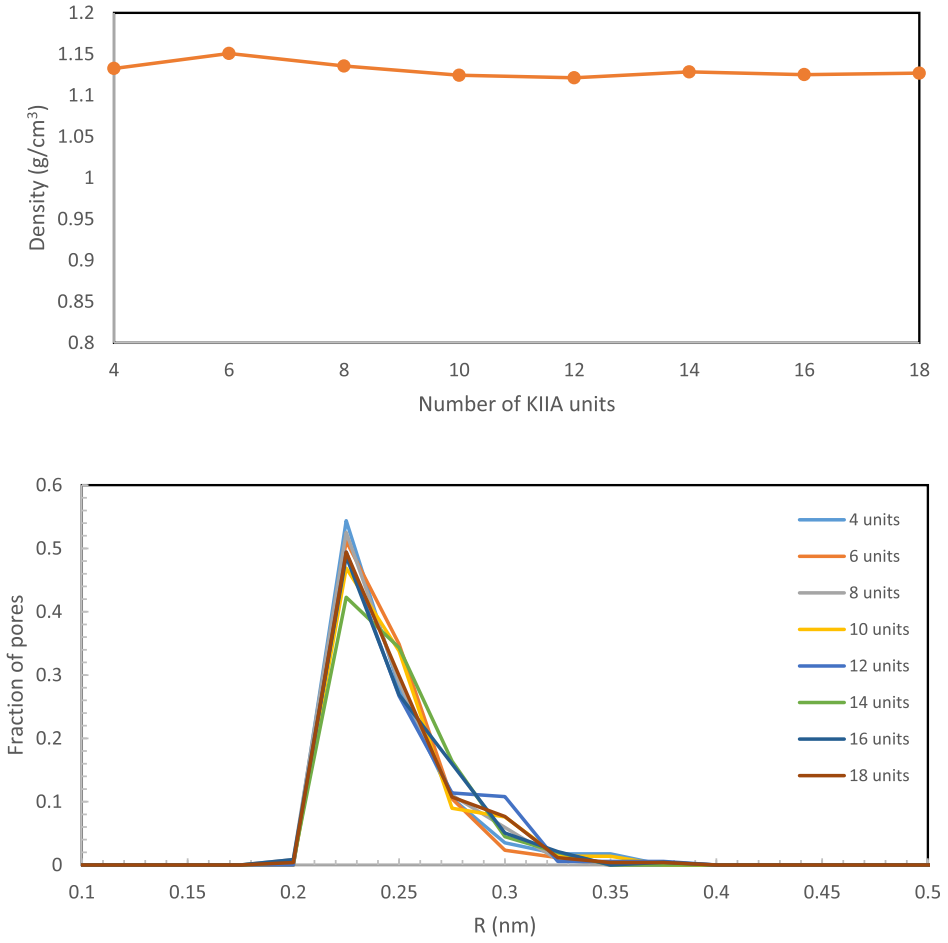

Figure 5. TOP: kerogen type IIA density as a function of the number of units. Bottom: PSD as a function of the number of units.

Table 2. Fugacity Data Used in the Adsorption Calculations

P (MPa)	fugacity (MPa)
2.067	2.028
3.445	3.340
6.890	6.494
10.335	9.503
20.670	18.056
41.340	35.842

atom types and charges. Similar to Compass and CFF93, the PCFF+ was introduced to complement the previous efforts of force fields capable of handling organic compounds. It has been applied successfully to reproduce some macroscopic properties reported in the literature, including the same kerogen prototypes used in this study.[27,28] A total of 8−12 units of kerogen were initially placed in a relatively large cell so that the density does not exceed 0.2 g/cm^3. The initialization of the system at the low density was followed to avoid any stability issues. Then, a large-scale atomic/molecular massively parallel simulator (LAMMPS) was employed to form the final kerogen structure.[29] The targeted temperature and pressure of the final configuration were selected to be 350 K and 20.67 MPa, respectively, in order to represent typical reservoir conditions. The molecular dynamics began with an initialization where a 3D periodic boundary, 9.5 cutoff value, and 2.0 skin were assigned. This was followed by an energy minimization stage to properly configure the molecular position and velocity. Next, a single stage of isochoric−isothermal *NVT* for 250 ps was performed at 900 K. At the same temperature, an isobaric−isothermal *NPT* stage was performed for 200 ps. Then, the temperature was reduced to 700, 500 K, and finally to 350 K in three consecutive *NPT* stages to form the final structure. The gradual decrease in temperature to the final targeted level assured structural stability during convergence. The final structures had densities of 1.0−1.3 g/cm^3, which were close to the values experimentally measured for the same types.[28] A summary of the molecular construction protocol is given in Figure 3.

Porosity and Pore Size Distribution. Gibbs Monte Carlo simulations for helium and the created kerogen structures were conducted to obtain the porosities of the six kerogens.

$$N_m = N_a - \rho_a V_P \quad (1)$$

where N_m and N_a are the number of excess and adsorbed molecules of helium, respectively; V_P is the pore volume; and ρ_a is the density of the helium. Under the assumption of zero excess molecules at such a degree of confinement, the above equation was used to estimate the pore volume. The porosity was then calculated by dividing the pore volume by the bulk volume.

Porosity, which is an indicator of the total pore volume, can be used to describe the total storage capacity of porous media. Detailed characterizations of pore volume, however, are needed to cast some light on the degree of confinement and underlying storage and transport mechanisms. For this purpose, PSD was extracted for all six nanoporous kerogen structures. PSD characterization was conducted by positioning nonoverlapping spheres at the vertices of the resulting polyhedral grid, with a

https://doi.org/10.1021/acsomega.1c00018
ACS Omega 2021, 6, 9549−9558

minimum threshold sphere radius of 0.2 nm (a sphere was created if its radius was greater than or equal to 0.2 nm).[30,31] The minimum threshold radius was selected based on the kinetic diameter of methane. A sample visual representation of the PSD calculations is given in Figure 4.

Representative Elementary Volume. To investigate the impact of the system size on the characteristics of the created structures, the construction of the kerogen, as described previously, was repeated with an increasing number of added macromolecule units. The final density and the PSD of each configuration were obtained as a function of the number of units. Sample analysis for type IIA is given in Figure 5. It can be seen that neither density nor PSD varied significantly for the considered configurations, suggesting that 8−12 units are sufficient to yield structures with consistent properties.

Adsorption Calculations. The six nanoporous structures developed were employed to host methane. Gibbs ensemble Monte Carlo simulation of the methane−kerogen interactions can be interpreted as the sorbed phase. The isotherm was selected to be at 350 K for pressure stages ranging from 300 to 6,000 psi (i.e., 2.067−41.340 MPa), which are representative of the profiles encountered in the field. At each stage, the Peng−Robinson equation of state was used to approximate the fugacity of methane (see Table 2).

The number of methane gas molecules hosted by the kerogen models was tracked through the Gibbs ensemble Monte Carlo calculations at different isothermal pressure stages, making it possible to plot the sorption profiles as a function of pressure for the six kerogen structures. A similar approach has been followed in prior studies.[32−34]

RESULTS AND DISCUSSION

Kerogen structure construction, porosity measurement, PSD characterization, and adsorption calculations were performed for the six kerogens listed in Table 1. It was the goal of this research to illustrate how kerogen petrophysics changes with the kerogen type and level of maturation. Hence, the analyses described in the previous section are presented and discussed below for three major kerogen types—IA, IIA, and IIIA—and for type II at different levels of maturity: IIA, IIB, IIC, and IID.

Kerogen Types. Helium pycnometry measurements revealed that the porosity was highest for kerogen type IIIA, followed by IIA and IA, in a descending order. The porosity trend observed was consistent with the PSD analysis, where kerogen type IIIA had the largest average pore size, followed by IIA and IA, in a descending order (see Table 3). Kerogen type IIIA had the highest content of aromatic carbon. The double and partial bonds associated with aromatic carbon are less flexible than single bonds. Aromatic carbon's higher resistance to folding may explain the relatively larger pores. Kerogen type IIA had the second highest aromatic carbon content of the three types. Its porosity was determined to be lower than type IIIA and higher than type IA. This was also consistent with the PSDs of the three types, as shown in Figures 6 and 7.

The ability of organic materials to host hydrocarbons is a vital characteristic that has significant implications for reservoir-scale reserve assessments. Methane adsorption capacity calculations described in the third section of the molecular approach were performed on the three kerogen types. The results are summarized in Figure 8.

The three types of kerogen exhibited voids of average 0.44−0.48 nm in diameter, as revealed by the PSD; such voids are capable of providing a single adsorption site for methane molecules (the kinetic diameter of methane is approximately 0.39 nm). The adsorption behavior showed results consistent with that of locations where Langmuir-like isotherms were obtained. Moreover, the isotherms in types IIA and IIIA showed sensitivity to an increase in porosity. The increased methane adsorption capacity signifies the role of shale gas and coalbed methane containing types II and III kerogens as indicating sources of natural gas.

Thermal Maturity. Kerogens of the same type can exist across a wide spectrum of thermal maturation. Below, kerogen's petrophysics are presented in the context of the maturity level for four type II structures in an ascending order of maturation: types IIA, IIB, IIC, and IID.

Table 3. Porosity and Maximum and Average Pore Sizes for Kerogen Types IA, IIA, and IIIA

structure	phi	*R*, max (nm)	*R*, avg (nm)
KIA	0.049	0.305	0.228
KIIA	0.056	0.313	0.231
KIIIA	0.076	0.379	0.239

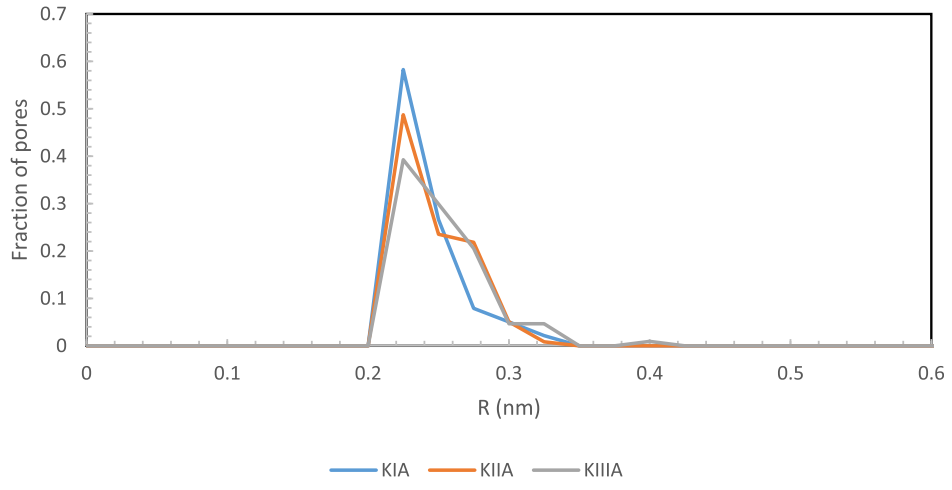

Figure 6. PSD for kerogen types IA, IIA, and IIIA.

https://doi.org/10.1021/acsomega.1c00018
ACS Omega 2021, 6, 9549−9558

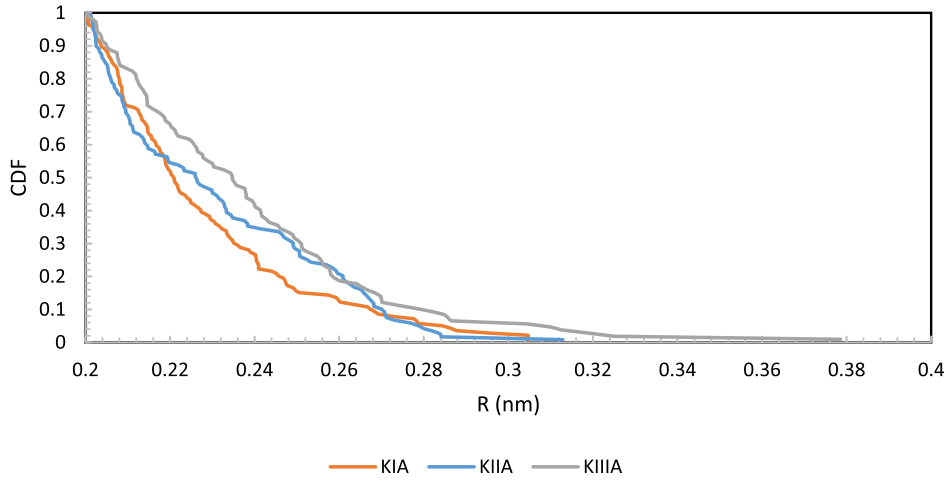

Figure 7. Cumulative distribution function of the PSD values for kerogen types IA, IIA, and IIIA.

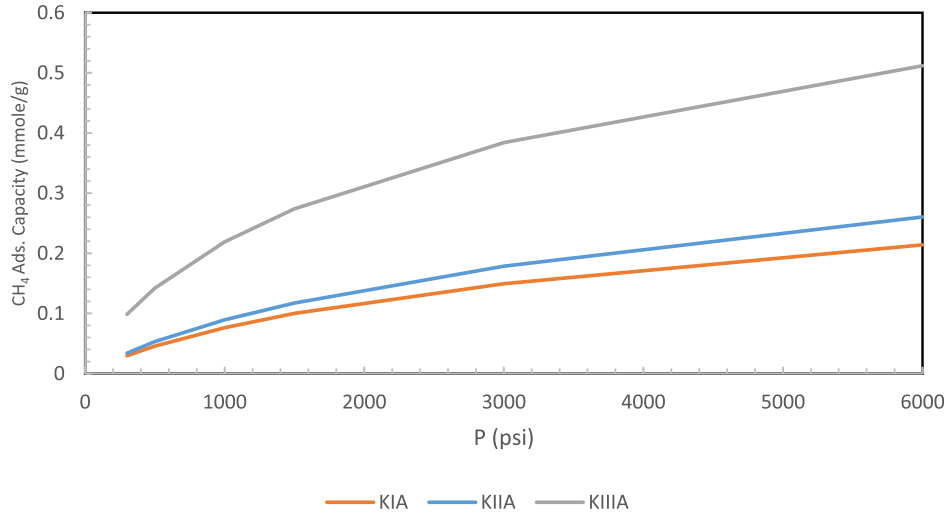

Figure 8. Methane adsorption capacity of kerogen types IA, IIA, and IIIA at 350 K.

Table 4. Porosities and Maximum and Average Pore Sizes for Kerogen Types IIA, IIB, IIC, and IID

structure	phi	*R*, max (nm)	*R*, avg (nm)
KIIA	0.056	0.313	0.231
KIIB	0.073	0.363	0.236
KIIC	0.075	0.461	0.234
KIID	0.144	0.507	0.257

Similar to the analyses described in the previous section, nanoporous structures were constructed, followed by extraction of PSD and helium pycnometry for porosity estimation; finally, methane adsorption calculations were carried out. The helium porosities are given Table 4, PSDs in Figures 9 and 10, and methane adsorption profile in Figure 11.

As the thermal maturity increased from type IIA to IID, porosity increased; it was highest for IID, followed by IIC, IIB, and IIA, in a descending order. The PSD showed consistent results, with type IID having largest pores and highest average pore size, followed by the others in the descending order of maturity. Intuitively, methane adsorption capacity would have the same trend as porosity. However, methane−kerogen interactions can also impact the adsorption. Methane is nonpolar, while kerogen can vary in the degree of polarity, with type IID being the most polar one. Among other immature kerogens, type IID is anticipated to have the least degree of affinity to methane from methane−carbon interaction point of view. Interestingly, kerogen type IID exhibited the highest methane adsorption capacity, implying the minimal role of polarity as compared to porosity. Similar adsorption characteristics have been reported in the literature.[35]

Storage and Transport Implications. The ability of kerogen macromolecules to form well-defined nanoporous structures is understood as the primary factor dictating methane adsorption capacity. In this context, porosity refers to the pore spaces formed between kerogen macromolecules and not those formed during pressure buildup or induced by tectonic movement. Hence, maximum adsorption capacity can be linked directly to the porosity of the kerogen, irrespective of the type and level of maturity. The maximum adsorption capacity of each kerogen structure and its corresponding porosity were extracted. The six sets of data points were used to plot the adsorption capacity versus porosity (see Figure 12).

A clear correlation can be seen between the adsorption capacity and porosity. It implies that the pore volume within kerogen structures is the primary parameter controlling the adsorption capacity. Such a relationship can serve as a means of

https://doi.org/10.1021/acsomega.1c00018
ACS Omega 2021, 6, 9549−9558

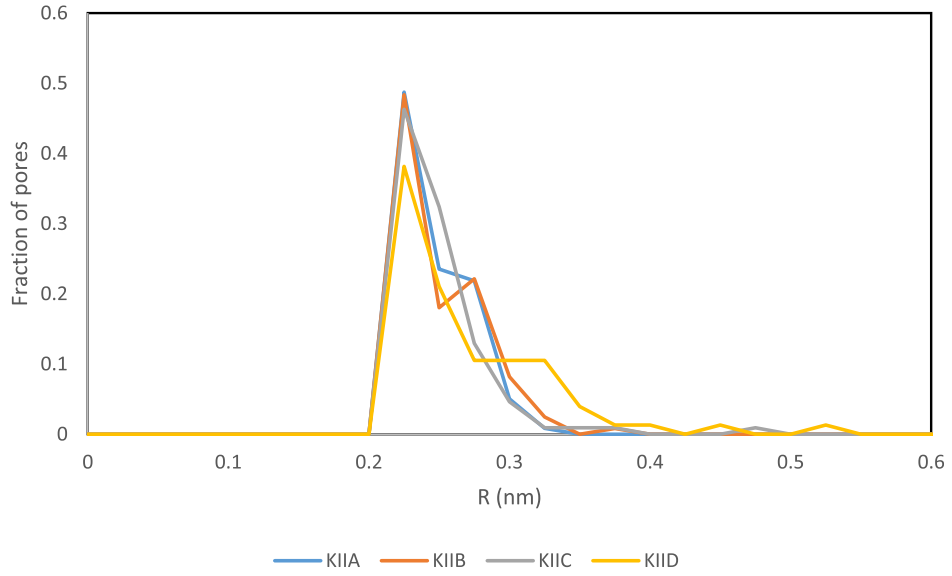

Figure 9. PSD for kerogen types IIA, IIB, IIC, and IID.

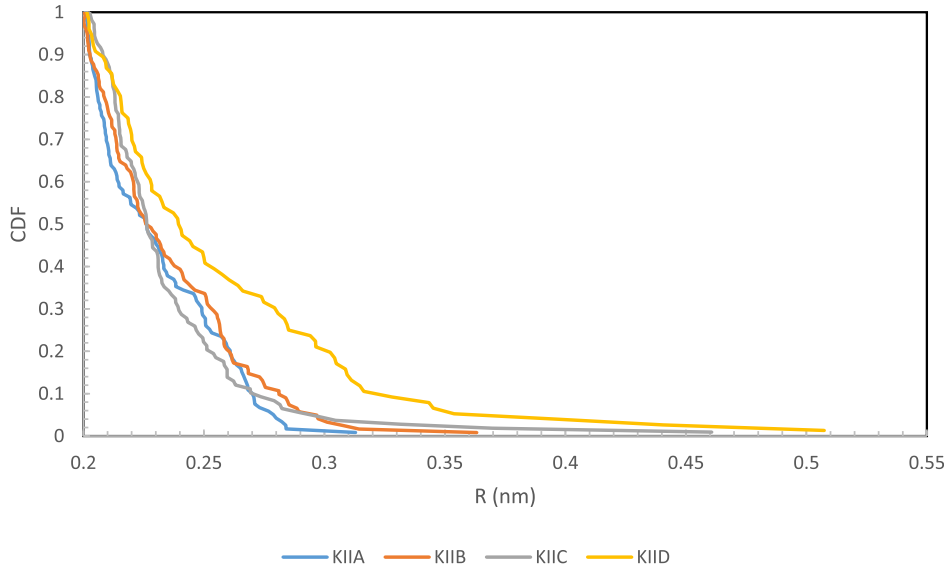

Figure 10. Cumulative distribution function of the PSD for kerogen types IIA, IIB, IIC, and IID.

deducing the storage capacity of organic materials, in terms of a measurable parameter (i.e., porosity).

$$C_{CH_4,max} = 36.42\phi^{1.7} \quad (2)$$

where $C_{CH4,max}$ is the maximum adsorption capacity of kerogen and ϕ is the porosity.

Conversely, transport is controlled by different regimes. The detailed characterization of PSD can shed some light on the predominant mechanism. The Knudsen number, which is defined as the ratio between the molecular mean free path λ to the characteristic pore size L, is an indicator of the transport mechanism. The Knudsen number Kn is given as

$$Kn = \frac{\lambda}{L} \quad (3)$$

The mean free path λ can be obtained through the kinetic theory of gases as

$$\lambda = \frac{k_B T}{\sqrt{2}\pi d^2 P} \quad (4)$$

where k_B is the Boltzmann's constant, T is the temperature, d is the kinetic diameter of the molecule (methane has a kinetic diameter of 0.39 nm), and P is the pressure. The Knudsen number is descriptive of the transport mechanism. In general:

- $Kn < 0.01$ continuum flow
- $0.1 > Kn > 0.01$ slip flow
- $10 > Kn > 1$ transition flow
- $Kn > 10$ free molecular diffusion

The characteristic pore size L was approximated for the six kerogen structures used in this study as the average pore size, allowing for the Knudsen number to be calculated for the structures as a function of pressure (see Figure 13). The Knudsen number for the pressure profile considered was within a range of 0.33−7.5, signifying transition flow as the predominant mechanism.

https://doi.org/10.1021/acsomega.1c00018
ACS Omega 2021, 6, 9549−9558

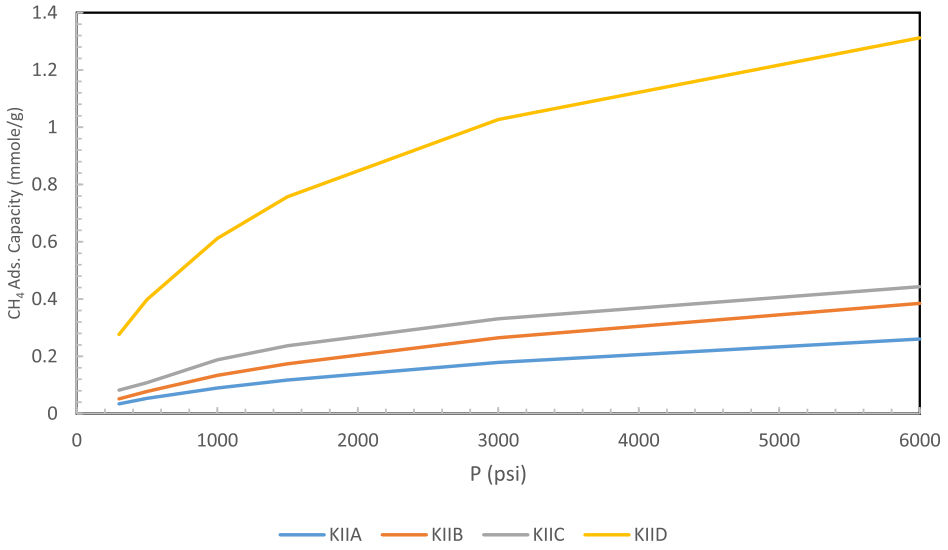

Figure 11. Methane adsorption capacity of kerogen types IIA, IIB, IIC, and IID at 350 K.

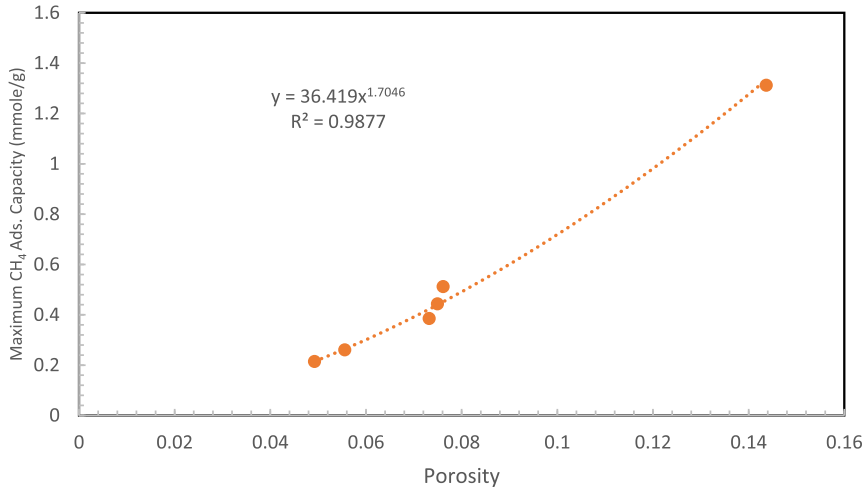

Figure 12. Maximum methane adsorption capacity of kerogen as a function of porosity; each porosity value corresponds to one of the six kerogen structures. Data were obtained at 41.34 MPa and 350 K.

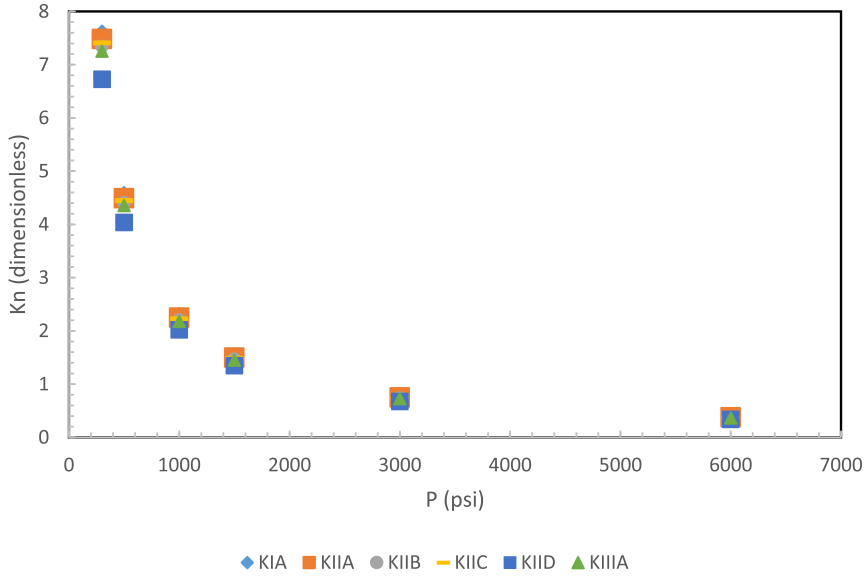

Figure 13. Knudsen number values for the six kerogen structures as a function of pressure and at a constant temperature of 350 K.

https://doi.org/10.1021/acsomega.1c00018
ACS Omega 2021, 6, 9549−9558

CONCLUSIONS

In this research, a molecular simulation approach was applied to investigate the petrophysical properties of kerogens of different origins and levels of maturation. Nanoporous kerogen structures were built from their respective single macromolecule units. Characterizations of porosity, PSD, and methane adsorption capacity were performed. Some conclusions can be drawn as follows:

- Kerogen petrophysics can vary among types. Type IIIA had the highest porosity, largest pores, and highest adsorption capacity, followed by IIA and IA, in a descending order.
- The petrophysics varies with maturity. The most mature structure had the highest porosity, followed by the others in a descending order of thermal maturity.
- Transition diffusion was found to be the predominant transport mechanism for all kerogen types, within a typical pressure range profile.

Experimental validation of these findings is recommended, as well as the extension of this analysis to other kerogen types.

AUTHOR INFORMATION

Corresponding Author

Saad Alafnan − *College of Petroleum Engineering and Geosciences, KFUPM, Dhahran 31261, Saudi Arabia;* orcid.org/0000-0001-9124-8340; Email: safnan@kfupm.edu.sa

Complete contact information is available at: https://pubs.acs.org/10.1021/acsomega.1c00018

Notes

The author declares no competing financial interest.

ACKNOWLEDGMENTS

The author acknowledges the support provided by the College of Petroleum Engineering and Geosciences (CPG) at the King Fahd University of Petroleum and Minerals in Saudi Arabia for the subscription granted to access the resource materials and journal articles reviewed in this work.

NOMENCLATURE

ϕ, porosity, dimensionless parameter
Kn, Knudsen number, dimensionless parameter
R, pore radius, nm
d, kinetic molecular diameter, *m*
L, characteristic pore size, m
k_B, Boltzmann constant, 1.38065×10^{-23} m^2kg/s^2K
T, temperature, K
P, pressure, psi, MPa, or Pa
V_P, pore volume, m^3
ρ_a, gas density, m^3/kg

REFERENCES

(1) Heller, R.; Vermylen, J.; Zoback, M. Experimental investigation of matrix permeability of gas shales. *AAPG Bull.* **2014**, *98*, 975−995.
(2) Alafnan, S. F. K.; Akkutlu, I. Y. Matrix-Fracture Interactions During Flow in Organic Nanoporous Materials Under Loading. *Transp. Porous Media* **2018**, *121*, 69−92.
(3) Curtis, E. M. Influence of thermal maturity on organic shale microstructure. 2013, http://www.ogs.ou.edu/MEETINGS/Presentations/2013Shale/2013ShaleCurtis.pdf.
(4) Zhou, S.; Yan, G.; Xue, H.; Guo, W.; Li, X. 2D and 3D nanopore characterization of gas shale in Longmaxi formation based on FIB-SEM. *Mar. Pet. Geol.* **2016**, *73*, 174−180.
(5) Klaver, J.; Desbois, G.; Littke, R.; Urai, J. L. BIB-SEM pore characterization of mature and post mature Posidonia Shale samples from the Hils area, Germany. *Int. J. Coal Geol.* **2016**, *158*, 78−89.
(6) Yang, C.; Zhang, J.; Han, S.; Xue, B.; Zhao, Q. Classification and the developmental regularity of organic-associated pores (OAP) through a comparative study of marine, transitional, and terrestrial shales in China. *J. Nat. Gas Sci. Eng.* **2016**, *36*, 358−368.
(7) Ambrose, R. J.; Hartman, R. C.; Diaz-Campos, M.; Akkutlu, I. Y.; Sondergeld, C. H. Shale gas-in-place calculations part I: new pore-scale considerations. *SPE J.* **2012**, *17*, 219−229.
(8) Tang, X.; Jiang, Z.; Jiang, S.; Wang, P.; Xiang, C. Effect of Organic Matter and Maturity on Pore Size Distribution and Gas Storage Capacity in High-Mature to Post-Mature Shales. *Energy Fuels* **2016**, *30*, 8985−8996.
(9) Zhang, Y.; He, Z.; Jiang, S.; Lu, S.; Xiao, D.; Chen, G.; Zhao, J. Factors Affecting Shale Gas Accumulation in Overmature Shales Case Study from Lower Cambrian Shale in Western Sichuan Basin, South China. *Energy Fuels* **2018**, *32*, 3003−3012.
(10) Guo, X.; Huang, Z.; Ding, X.; Chen, J.; Chen, X.; Wang, R. Characterization of Continental Coal-Bearing Shale and Shale Gas Potential in Taibei Sag of the Turpan-Hami Basin, NW China. *Energy Fuels* **2018**, *32*, 9055−9069.
(11) Down, A. L.; Himus, G. W. A preliminary study of the chemical constitution of kerogen. *J. Inst. Petrol.* **1941**, *27*, 426−445.
(12) Forsman, J. P.; Hunt, J. M. Insoluble organic matter (kerogen) in sedimentary rocks. *Geochim. Cosmochim. Acta* **1958**, *15*, 170−182.
(13) van Krevelen, D. W. *Coal: Typology—Chemistry—Physics—Constitution*, 1st ed.; Elsevier: The Netherlands, 1961.
(14) Durand, B.; Espitalié, J. Evolution de la matière organique au cours de l'enfouissement des sédiments. *Comptes Rendus Acad. Bulg. Sci.* **1973**, *276*, 2253−2256.
(15) Tissot, B. P.; Durand, B.; Espitalie, J.; Combaz, A. Influence of nature and diagenesis of organic matter in formation of petroleum. *Am. Assoc. Petrol. Geol. Bull.* **1973**, *57*, 809.
(16) Durand, B.; Nicaise, G.; Roucaché, J.; Vandenbroucke, M.; Hagemann, H. W. Etude géochimique d'une série de charbons. In *Advances in Organic Geochemistry*; Campos, R., Goñi, J., Eds.; ENADIMSA: Madrid, 1975; pp 601−631.
(17) Tissot, B.; Vandenbroucke, M. Geochemistry and pyrolysis of oil shales. In *Geochemistry and Chemistry of Oil Shales, ACS Symposium Series*; Miknis, F. P., McKay, J. F., Eds; American Chemical Society: Washington D.C, 1983; vol. *230*, pp 1−11.
(18) Albrecht, P.; Vandenbroucke, M.; Mandengué, M. Geochemical studies on the organic matter from the Douala Basin (Cameroon)-I. Evolution of the extractable organic matter and the formation of petroleum. *Geochim. Cosmochim. Acta* **1976**, *40*, 791−799.
(19) Forsman, J. P. Geochemistry of kerogen. In *Organic Geochemistry, Earth Series Monograph*; Breger, I. A., Ed.; Pergamon Press: Oxford, 1963; vol. *16*, pp 148−182.
(20) Burlingame, A. L.; Haug, P. A.; Schnoes, H. K.; Simoneit, B. R. Fatty acids derived from the Green River Formation oil shale by extractions and oxidations—a review. In *Advances in Organic Geochemistry*; Schenck, P. A., Havenaar, I., Eds.; Pergamon Press: Oxford, 1969; pp 85−129.
(21) Djuricic, M.; Murphy, R. C.; Vitorovic, D.; Biemann, K. Organic acids obtained by alkaline permanganate oxidation of kerogen from the Green River (Colorado) shale. *Geochim. Cosmochim. Acta* **1971**, *35*, 1201−1207.
(22) Yen, T. F. Structural aspects of organic components in oil shales. In *Oil Shale, Developments in Petroleum Science*; Yen, T. F., Chilingarian, G. V., Eds.; Elsevier: Amsterdam, 1976; vol. *5*, pp 129−148.
(23) Tissot, B.; Deroo, G.; Hood, A. Geochemical study of the Uinta Basin: formation of petroleum from the Green River formation. *Geochim. Cosmochim. Acta* **1978**, *42*, 1469−1485.

(24) Vandenbroucke, M.; Largeau, C. Kerogen origin, evolution and structure. *Org. Geochem.* **2007**, *38*, 719−833. http://www.sciencedirect.com/science/article/pii/S014663800700006X
(25) Vandenbroucke, M. Structure of kerogens as seen by investigations on soluble extracts. In *Kerogen, Insoluble Organic Matter from Sedimentary Rocks*; Durand, B., Ed.; Editions Technip: Paris, 1980; pp 415−443.
(26) Behar, F.; Vandenbroucke, M. Chemical modelling of kerogens. *Org. Geochem.* **1987**, *11*, 15−24.
(27) Ungerer, P.; Rigby, D.; Leblanc, B.; Yiannourakou, M. Sensitivity of the aggregation behaviour of asphaltenes to molecular weight and structure using molecular dynamics. *Mol. Simulat.* **2014**, *40*, 115−122.
(28) Ungerer, P.; Collell, J.; Yiannourakou, M. Molecular Modeling of the Volumetric and Thermodynamic Properties of Kerogen: Influence of Organic Type and Maturity. *Energy Fuels* **2014**, *29*, 91−105.
(29) Plimpton, S. Fast parallel algorithms for short-range molecular dynamics. *J. Comput. Phys.* **1995**, *117*, 1−19.
(30) Barber, C. B.; Dobkin, D. P.; Huhdanpaa, H. The Quickhull Algorithm for Convex Hulls. *ACM Trans. Math Software* **1996**, *22*, 469−483.
(31) Aljaberi, J.; Alafnan, S.; Glatz, G.; Sultan, A. S.; Afagwu, C. The Impact of Kerogen Tortuosity on Shale Permeability. *SPE J.* **2020**, 1.
(32) Alafnan, S.; Falola, Y.; Al Mansour, O.; Alsamadony, K.; Awotunde, A.; Aljawad, M. Enhanced Recovery From Organic-Rich Shales through Carbon Dioxide Injection: Molecular-Level Investigation. *Energy Fuels* **2020**, *34*, 16089.
(33) Alafnan, S.; Solling, T.; Mahmoud, M. Effect of Kerogen Thermal Maturity on Methane Adsorption Capacity: A Molecular Modeling Approach. *Molecules* **2020**, *25*, 3764.
(34) Alafnan, S.; Sultan, A. S.; Aljaberi, J. Molecular Fractionation in the Organic Materials of Source Rocks. *ACS Omega* **2020**, *5*, 18968.
(35) Yang, Y.; Liu, J.; Yao, J.; Kou, J.; Li, Z.; Wu, T.; Zhang, K.; Zhang, L.; Sun, H. Adsorption behaviors of shale oil in kerogen slit by molecular simulation. *Chem. Eng. J.* **2020**, *387*, 124054.

https://doi.org/10.1021/acsomega.1c00018
ACS Omega 2021, 6, 9549−9558